FOI
SWEDISH DEFENCE
RESEARCH AGENCY

FOI-R--0130--SE
June 2001
ISSN 1650-1942
Base data report

Christer Fureby, Henrik Almström

Hull Induced Noise.

Part 1: Hydrodynamic Noise Produced by the Turbulent Flow around a Rigid Hull

Weapons and Protection
SE-147 25 TUMBA

SWEDISH DEFENCE RESEARCH AGENCY

Weapons and Protection
SE-147 25 Tumba

FOI-R--0130--SE

June 2001

ISSN 1650-1942

Base data report

Christer Fureby, Henrik Almström

Hull Induced Noise. Part 1: Hydrodynamic Noise Produced by the Turbulent Flow around a Rigid Hull

Issuing organization	Report number, ISRN	Report type
FOI – Swedish Defence Research Agency Weapons and Protection SE-147 25 Tumba	FOI-R--0130--SE	Base data report
	Research area code 4. C4ISR	
	Month year June 2001	**Project no.** E2009
	Customers code 1. Research for the Government	
	Sub area code 43 Underwater Surveillance Sensors	

Author/s (editor/s)	Project manager
Christer Fureby Henrik Almström	Paul Ström
	Approved by
	Scientifically and technically responsible Christer Fureby

Report title

Hull Induced Noise. Part 1: Hydrodynamic Noise Produced by the Turbulent Flow around a Rigid Hull

Abstract (not more than 200 words)

Surface ships, submarines and other submersibles all have a hydroacoustic signature that is revealing for passive sonar in stationary and mobile surveillance systems, and may also interfere with the ship's own sonar. The sources of the hydroacoustic signature can be divided into internal and external sources. The internal sources mainly consist of onboard machinery whilst the external sources mainly consist of the hydrodynamic noise, i.e. the sound from the turbulent boundary layer. The internal sources depend on the operating conditions and the tactical situation, and advanced signature reduction has been used for a long time. As regards the external sources not much has been done due to the lack of knowledge about the fluid dynamics and the prediction methods. The present study is divided into two parts where part 1 is a contribution towards a better understanding of the fundamental physics of hydrodynamic noise produced by the turbulent flow around a rigid hull, whereas part 2 focuses on hydrodynamic noise produced by a vibrating hull excited by the turbulent flow. A methodology is here developed to predict the sound radiated by a surface ship, a submarine or other underwater vehicles, based on splitting the computation into a viscous incompressible flow simulation model, using Large Eddy Simulations, and a separate acoustic calculation. Such a two-step approach is particularly attractive for a nearly incompressible flow, since a fully compressible simulation of a virtually incompressible flow is both too expensive (since the acoustic time scales need to be properly resolved) and unnecessarily complicated. Finally, we apply this calculation procedure to the flow around a prolate spheroid in order to demonstrate the method. Qualitative or quantitative comparison with experimental data is planned in a future study.

Keywords

flow induced noise, LES

Further bibliographic information	Language English
ISSN 1650-1942	**Pages** 23 p.
	Price acc. to pricelist **Security classification**

Utgivare	Rapportnummer, ISRN	Klassificering
Totalförsvarets Forskningsinstitut - FOI Vapen och skydd 147 25 Tumba	FOI-R--0130--SE	Underlagsrapport
	Forskningsområde 4. Spaning och ledning	
	Månad, år Juni 2001	**Projektnummer** E2009
	Verksamhetsgren 1. Forskning för regeringens behov	
	Delområde 43 Undervattenssensorer	

Författare/redaktör	Projektledare
Christer Fureby Henrik Almström	Paul Ström
	Godkänd av
	Tekniskt och/eller vetenskapligt ansvarig Christer Fureby

Rapportens titel (i översättning)

Skrovinducerat buller. Del 1: Strömningsinducerat buller orsakat av det turbulenta strömningsfältet omkring ett stelt skrov.

Sammanfattning (högst 200 ord)

Ytfartyg, ubåtar och andra undervattensfarkoster har hydroakustiska signaturer som är röjande för passiv sonar i stationära och rörliga övervakningssystem. Dessa signaturer kan dessutom störa fartygets egen sonar. Källorna till den hydroakustiska signaturen kan delas upp i interna och externa källor. De interna källorna utgörs huvud-sakligen av maskineri, medan de externa källorna främst består av hydrodynamiskt buller, dvs. ljudet från det turbulenta gränsskiktet. De inre källorna beror på driftsförhållandena och den taktiska situationen, och avancerad signaturreduktion har använts under lång tid. Beträffande de externa källorna har mycket litet blivit gjort på grund av bristen på kunskap om strömningsmekaniken och simuleringsmetoder. I föreliggande studie syftar del 1 till att ge en bättre förståelse av den grundläggande fysiken hos hydrodynamiskt buller genererat av den turbulenta strömningen kring det stela skrovet. Del 2 behandlar hydrodynamiskt buller som genereras av ett vibrerande skrov förorsakat av den turbulenta strömningen. Här utvecklas en metodik för att prediktera det utstrålade bullret från ett ytfartyg, en ubåt eller andra undervattensfarkoster utifrån en uppdelning av beräkningen i en viskös in-kompressibel del, baserad på ”Large Eddy Simulering”, och en separat akustisk beräkning. En sådan tvåstegs-metodik är speciellt attraktiv för nära inkompressibel strömning eftersom en kompressibel simulering av en nära inkompressibel strömning är både för dyr (eftersom de akustiska tidsskalorna måste bli upplösta) och för komplicerad. Slutligen använder vi denna beräkningsmodell vid strömningen kring en rotationsellipsoid i syfte att demonstrera metoden. Kvalitativa och kvantitativa jämförelser med experimentella akustiska data planeras i en framtida studie.

Nyckelord

strömningsinducerat buller, LES

Övriga bibliografiska uppgifter	Språk Engelska
ISSN 1650-1942	**Antal sidor:** 23 s.
Distribution enligt missiv	**Pris: Enligt prislista** **Sekretess**

Contents

Excecutive Summary

Surface ships, submarines and other submersibles all have a hydroacoustic signature that is revealing for passive sonar in stationary and mobile surveillance systems, and may also interfere with the ship's own sonar. The sources of the hydroacoustic signature can be divided into internal and external sources. The internal sources mainly consist of onboard machinery whilst the external sources mainly consist of the hydrodynamic noise, i.e. the sound from the turbulent boundary layer. The internal sources depend on the operating conditions and the tactical situation, and advanced signature reduction has been used for a long time. Considering the external sources not much has been done due to the lack of knowledge about the fluid dynamics and the prediction methods. The present study is divided into two parts where part 1 is a contribution towards a better understanding of the fundamental physics of hydrodynamic noise produced by the turbulent flow around a rigid hull whereas part 2 focuses on hydrodynamic noise produced by a vibrating hull excited by the turbulent flow. Because of the prohibitive cost of direct calculation of noise or sound from the Navier Stokes Equations and the conflicting requirements for the accurate calculation of both the viscous flow and the acoustic field, it is necessary to perform a two-step calculation, where the flow field is calculated separately from the acoustic field. Such a two-step approach is particularly attractive for a nearly incompressible flow, since a fully compressible simulation of a virtually incompressible flow is both too expensive (since the acoustic time scales need to be properly resolved) and unnecessarily complicated. The approach that will be taken here is based on that the flow field is evaluated in the first step using Large Eddy Simulations (LES) where the acoustic perturbations are neglected. In the second step, equations for the acoustic variables are solved. These equations are here derived from first principles by decomposing all variables into incompressible and acoustic components. The resulting model consists in an ordinary incompressible LES flow model from which the flow is obtained, and equations for the acoustic components, from which a source term to the wave-equation of the pressure is obtained. Separate simulation models for solving this wave-propagation problem, taking into account environmental effects, complex geometrical as well as physical boundary conditions, have been developed by others. Finally, we apply this calculation method to the flow around a prolate spheroid in order to demonstrate the method. Qualitative or quantitative comparison with experimental data is planned in a future study.

1. Introduction

Surface ships, submarines and other submersibles all have a hydroacoustic signature that is revealing for passive sonar in stationary and mobile surveillance systems, such as the sonar of a submarine, and also interferes with the ship's or submarine's own sonar. The sea-state and the environmental factors of the sea contribute to the fact that the range of the signature can be very extensive, especially during certain seasons. The hydroacoustic signature is used also in minesensors and in passive torpedo homing devises, which detects, classifies and positions the target. Advanced signal processing methods have been developed for this purpose. Hence the weapons effect can be optimized and a mobile weapon can be guided to the target. The sources of the hydroacoustic signature can be divided into internal and external sources. The internal sources mainly consists of onboard machinery, such as pumps, valves, generators and engines, whereas the external sources mainly consists of the hydrodynamic noise, i.e. the sound that is being produced by the turbulent boundary layer and wake in the vicinity of the hull, and the propulsor. Furthermore, the turbulent boundary layer may also excite the ship itself causing noise which propagates in the surrounding fluid. As regards the internal sources, the levels and frequencies of the internal sound sources depends critically on the operating conditions and the tactical situation. Advanced signature reduction has been used for a long time on submarines, and has recently also been introduced on surface ships. Machinery is isolated from vibrations, sometimes with elastic fittings and covering hoods to reduce the transmission of sound. Considering the external sources not much has been done due to the lack of knowledge about the basic physical phenomenon, such as boundary layer turbulence, and our inability to investigate these effects, either experimentally or theoretically, [1]. The present study, part 1, is a contribution towards better understanding of the fundamental physics of hydrodynamic noise produced by the turbulent flow around a rigid hull, whereas part 2 focuses on hydrodynamic noise produced by a vibrating hull excited by the turbulent flow.

An accurate prediction of the sound radiated by a surface ship, a submarine or other underwater vehicles requires a method capable of reproducing the near-field turbulence dynamics with sufficient fidelity to allow the direct evaluation of the non-compact (i.e. distributed) sound sources. Obviously, Reynolds Averaged Numerical Simulations (RANS) based methods require too much empirical input and are not suitable to accurately describe the distribution of the acoustic sources in space and time. A great deal of recent understanding of turbulence physics in viscous wall-bounded flows has emerged from Direct Numerical Simulations (DNS) at low Reynolds (Re) numbers. However, as DNS is restricted to Re-numbers well below the values of ship and submarine hydrodynamics, LES techniques appear to be the only realistic available tool to obtain the necessary near-field flow data upon which to base the prediction of sound emitted by turbulent boundary layers and wakes, which dominate ship hydrodynamics. Though still significantly more expensive than RANS methods, LES offers the advantage that little or no empirical input is required, which is a significant advantage when one is interested in a robust method to predict the radiated sound field. This should allow us to better understand the role of coherent structures to the noise generation. The fact that the sound spectrum is dominated by the contribution of the large coherent structures justifies the use of LES as a base for noise calculations. However, at very high Re-numbers the contribution of the smaller scales to the sound spectrum may be non-negligible in the range of the frequencies of interest, and this problem is yet to be investigated.

Over the last decade LES techniques have advanced to a point where they have been shown to predict complex flows (characterized by a large disparity between the different spatial and temporal turbulent scales) fairly accurately, [2-4]. The use of LES for aeroacoustics problems, [5-6],

and hydroacoustics applications is a natural development which presents new challenges. The major challenge is related to the large disparity which exists between the energy levels associated with the fluctuations from the large-scale turbulent motions and those associated with the acoustic fluctuations. As most of the acoustic sources are situated within the boundary layer, a first requirement is to simulate correctly this flow to be able to calculate accurately the distribution and strength of the acoustic sources. Only the information about the high-frequency turbulence, and hence its associated sound is lost in LES, due to the inherent low-pass filtering. Furthermore, no simplifying assumptions about the acoustic wave propagation are required. The only difficulty is numerical – accurate simulations of sound waves, especially in complex confinements such as littoral waters, concomitantly with the flow structures of the underlying turbulent flow is a considerable task. An important consequence is that accurate prediction of the radiated flow induced noise requires the use of numerical schemes with low dispersion and dissipation errors. Moreover, the quality of the noise data can be easily compromised by the boundary layer treatment. Higher Re-number and coarser grids put, in turn, a higher burden on the robustness and accuracy of the numerical methods used in aeroacoustic or hydroacoustic simulations. This is why attempts to simulate submarine or ship hydrodynamics and their radiated noise using LES is quite recent.

Most classical approaches in aero- and hydroacoustics are based on solving a wave-equation of the form $c_0^{-2}\partial_t^2 p' - \mathrm{div}(\mathrm{grad}p') = K$, where c_0 is the ambient speed of sound, p' the acoustic pressure fluctuations and K a source term taking non-zero values only outside of the boundary layer. In Blake, [1], different methods are discussed for modelling the term K. One of these models dates back to the pioneering works of Corcos, [7], where closure models for K are formulated entirely from experimental data. Most other models discussed in [1] are also related to experimental data. Not only until recently, methods based on first principles have been used for determining K, e.g., [8-9]. In particular, the field of aeroacoustics has been pioneering in using high-level computational fluid dynamic methods, involving RANS, LES and even DNS, for calculating the sound emission properly, cf. [10-11], but considering virtually incompressible flows not much have been done, mainly due to the technical (i.e. computational) problems previously discussed.

The outline of the present report is as follows. First we give an overview of the state-of-the-art in turbulent flow modeling in order to review the current simulation models, and their abilities. Then we derive a hydroacoustic computational model based on splitting the calculation into separate viscous and acoustic simulation models. Following this we discuss the numerical methods required for solving viscous problem in the context of LES and the associated acoustic problem. After this we present a computational example – the flow past a prolate spheroid at incidence. Simulation data are compared to experimental data in order to validate the LES model. Unfortunately, no data is available for comparison of the acoustic calculation. Finally, some concluding remarks are presented together with a brief discussion of future work related to hydroacoustics.

2. Turbulent Flow Modeling

Computational Fluid Dynamics (CFD) is accomplished by numerical solution of the Navier-Stokes Equations (NSE), which are the governing equations of fluid flow, [12]. These equations consist of conservation and balance laws for mass and momentum supplemented by constitutive equations for a Newtonian fluid. Numerical solution is currently the only practical way of solving the NSE due to their non-linearity and corresponding extensive range of eddy scales. The ratio of the largest eddies (with characteristic size λ_l) to the smallest Kolmogorov eddies (with size λ_K) can be related

to the Reynolds (Re) number, i.e. the ratio of inertial to viscous forces, as $\lambda_I/\lambda_K=Re^{3/4}$. This implies that the number of degrees of freedom required in a Direct Numerical Simulation (DNS), in which all scales are resolved, scale as $Re^{9/4}$. For high Re-numbers, present-day computers are not powerful enough to handle such problems and thus alternative methods have to be devised for turbulent flow simulations. In order to handle the wide spectrum of eddy scales we need to reduce the number of degrees of freedom. The common way of doing this is by means of RANS, [13]. Here, equations for a statistical average $\langle\cdot\rangle$ of the variables are accomplished by averaging the NSE over homogeneous directions, time or across an ensemble of equivalent flows. Since most engineering flows involve inhomogeneous flow time averaging is most appropriate. The turbulent fluctuations are not represented directly by the simulation but are included by way of a turbulence model. This averaging makes it possible to reduce the number of scales (i.e. degrees of freedom) considerably. The statistical character of RANS prevents a detailed description of the physical mechanisms, and it is thus unsuitable for problems where the fluid dynamic details are important. On the other hand, RANS is appropriate for analyzing performance characteristics as long as the turbulence models are able to represent the turbulent stresses sufficiently. The most advanced turbulence modeling method at hand is LES, [14-15]. In LES a separation between large supergrid and small subgrid scales is imposed by means of a spatial filtering related to the characteristic size of the grid – Δ. The effects of the subgrid scales on the supergrid scales are accounted for by way of a model – a subgrid model. LES contains more information of the flow than RANS but is also more expensive and is not presently suitable for screening of design parameters but rather for detailed studies and to gain qualitative and quantitative understanding of phenomena.

In LES, the motion is separated into small and large eddies and equations are solved for the latter. The separation is achieved by means of a low-pass filter, for further details see [16]. For an incompressible viscous fluid, the LES-equations are obtained from the NSE by convoluting the latter by a pre-defined filter kernel $G=G(\mathbf{x},\Delta)$, so that the LES equations becomes,

$$\begin{cases} \mathrm{div}(\bar{\mathbf{v}})=0, \\ \partial_t(\bar{\mathbf{v}})+\mathrm{div}(\bar{\mathbf{v}}\otimes\bar{\mathbf{v}})=-\mathrm{grad}\bar{p}+\mathrm{div}(\bar{\mathbf{S}}-\mathbf{B})+\bar{\mathbf{f}}, \end{cases} \tag{1}$$

where $\mathbf{v}$ is the velocity, p the pressure, $\mathbf{S}=2\nu\mathbf{D}$ the viscous stress tensor, $\mathbf{D}=\frac{1}{2}(\mathbf{L}+\mathbf{L}^T)$ the rate-of-strain tensor, ν the viscosity, $\mathbf{L}=\mathrm{grad}\mathbf{v}$ and $\mathbf{f}$ the body force. Specific to LES is the resolved components, denoted by an overbar and the subgrid scale stress tensor $\mathbf{B}=(\overline{\mathbf{v}\otimes\mathbf{v}}-\bar{\mathbf{v}}\otimes\bar{\mathbf{v}})$. The subgrid stress tensor $\mathbf{B}$ represents the effects of the subgrid flow on the resolved flow, and must be modeled using information from the resolved flow prior to discretization at a resolution near Δ – more affordable than DNS. Such models must, in absence of a universal theory of turbulence, include rational use of empirical information. Presently, two modeling strategies exist: *Functional modeling* consists in modeling the action of the subgrid scales on the resolved scales. This is basically of energetic nature so that the balance of the energy transfers between the two scale ranges is sufficient to describe the subgrid scale effects. *Structural modeling* consists of modeling $\mathbf{B}$ without incorporating any knowledge of the nature of the interactions between the subgrid and the resolved scales. Such models can be based either on series expansion techniques, transport equations, scale similarity or other deterministic approaches. These methods are different and each contains individual classes of subgrid models. For the purpose of this study we use functional modeling in which the energy transfer mechanism from the resolved to the subgrid scales is assumed analogous to that of a Brownian motion superimposed on the motion of the resolved scales. Hence,

$$\mathbf{B}_D = \mathbf{B} - \tfrac{1}{3}(\mathrm{tr}\mathbf{B})\mathbf{I} = -2\nu_k \overline{\mathbf{D}}, \tag{2}$$

where $\mathbf{B}_D$ is the deviatoric part of $\mathbf{B}$ and ν_k is the subgrid viscosity. The non-deviatoric part $\frac{1}{3}\mathrm{tr}\mathbf{B}$ is added to the filtered pressure $\overline{p}$, and does thus not require modeling in the incompressible case. Thus, the generalized pressure $\overline{\pi}=\overline{p}+\frac{2}{3}k$ and the filtered pressure $\overline{p}$ may be different when k becomes large. To close (2) we need models for ν_k and k, and for this we assume the existence of characteristic length and velocity scales and we infer total separation between resolved and subgrid scales. Hence, $\nu_k=\nu_k(\Delta,k,\varepsilon,E)$, where ε is the dissipation of k, and $E=E(|\mathbf{k}|)$, with $\mathbf{k}$ being the wavenumber vector, represents the shape of the spectrum. For a Kolmogorov spectrum,

$$\nu_k = c_\alpha \varepsilon^{\alpha/3} k^{(\alpha-1)/2} \Delta^{1+\alpha/3}, \tag{3}$$

where $c_\alpha = A/(K_0\pi^{4/3})(3K_0/2)^{(\alpha-1)/2}\pi^{(1-\alpha)/3}$, with $K_0 \approx 1.5$, $A \approx 0.4$ and α is a parameter to be varied. Interesting forms of ν_k can be obtained for different α-values. For $\alpha=1$ we obtain $\nu_k = c_1\varepsilon^{1/3}\Delta^{4/3}$, which in conjunction with $\varepsilon = c_\varepsilon'\Delta^2\|\overline{\mathbf{D}}\|^3$ yields the Smagorinsky model (SMG) $\nu_k = c_D\Delta^2\|\overline{\mathbf{D}}\|$, with $c_D=0.03$, [17]. For $\alpha=0$, $\nu_k = c_k\Delta k^{1/2}$, where $c_k=0.06$. This model only uses k, which is a subgrid quantity, and ensures that ν_k will be zero if the flow is well resolved, and thus offers better physical consistency than the subgrid models based on the resolved scales. Different ways can be used to determine k: e.g. in the One-Equation Eddy Viscosity Model (OEEVM), [18-19],

$$\partial_t(k) + \mathrm{div}(k\mathbf{v}) = -\mathbf{B}\cdot\overline{\mathbf{D}} + \mathrm{div}((\nu+\nu_k)\mathrm{grad}k) + c_\varepsilon' k^{3/2}/\Delta, \tag{4}$$

in which the diffusion term is modeled by a gradient hypothesis whilst the dissipation term is modeled using dimensional arguments, e.g. [18].

3. Mathematical Modeling of Hydrodynamic Noise

In attempting to develop a computational hydroacoustic technique several questions arise which are less critical in other applications of computational fluid dynamics. Among these we can mention: (i) The small amplitudes of the acoustic variables relative to other variables in the flow; (ii) The high frequencies of interest; (iii) The need for long time solutions to obtain adequate spectral resolution; (iv) The different numerical and computational requirements required for simultaneous viscous solution (i.e. high spatial and temporal resolution) and acoustic wave tracking (i.e. large computational domains and long time solutions) are contradictory. Hence, because of the prohibitive cost of direct calculation of noise or sound from the NSE, and the conflicting requirements for the accurate calculation of both the viscous flow and the acoustic field, it is, if possible, to perform a two-step calculation, where the flow field is calculated separately from the acoustic field. Such a two-step approach is particularly attractive for incompressible flow, since a fully compressible simulation of a virtually incompressible flow is both too expensive (since the acoustic time scales needs to be properly resolved) and unnecessarily complicated. The approach that will be taken here is based on that the flow field are evaluated in the first step using LES where the acoustic perturbations are neglected. In the second step, equations for the acoustic variables are solved.

The LES-equations for a compressible viscous fluid can be formulated using density-weighted or Favré filtering, in which $\tilde{\Phi}=\overline{\rho\Phi}/\overline{\rho}$ where Φ is any variable, in the following form,

$$\begin{cases} \partial_t(\bar{\rho})+\mathrm{div}(\bar{\rho}\tilde{\mathbf{u}})=0, \\ \partial_t(\bar{\rho}\tilde{\mathbf{u}})+\mathrm{div}(\bar{\rho}\tilde{\mathbf{u}}\otimes\tilde{\mathbf{u}})=-\mathrm{grad}\bar{p}+\mathrm{div}(\overline{\mathbf{S}_u}-\mathbf{B}_u)+\bar{\rho}\tilde{\mathbf{f}}, \\ \partial_t(\bar{\rho}\tilde{\varepsilon})+\mathrm{div}(\bar{\rho}\tilde{\mathbf{u}}\tilde{\varepsilon})=-\overline{p\mathrm{div}\mathbf{u}}+\overline{\mathbf{S}_u\cdot\mathrm{grad}\mathbf{u}}+\mathrm{div}(\bar{\mathbf{h}}-\mathbf{b})+\bar{\rho}\tilde{\sigma}, \end{cases} \tag{5}$$

where ρ is the density, $\mathbf{u}$ the (compressible) velocity, $\mathbf{S}_u=(\lambda+\frac{2}{3}\mu)\mathrm{div}\mathbf{u}+\mu(\mathrm{grad}\mathbf{u}+\mathrm{grad}\mathbf{u}^T)$ the viscous stress tensor, p the pressure, $\mathbf{B}_u=\bar{\rho}(\widetilde{\mathbf{u}\otimes\mathbf{u}}-\tilde{\mathbf{u}}\otimes\tilde{\mathbf{u}})$ the subgrid stress tensor, $\mathbf{f}$ the specific body force (which will be neglected), ε the internal energy, $\overline{p\mathrm{div}\mathbf{u}}$ the pressure-dilatation, $\overline{\mathbf{S}_u\cdot\mathrm{grad}\mathbf{u}}$ the dissipation function, $\bar{\mathbf{h}}=\kappa\mathrm{grad}\tilde{T}$ the heat flux vector, $\mathbf{b}=\bar{\rho}(\widetilde{\mathbf{u}\varepsilon}-\tilde{\mathbf{u}}\tilde{\varepsilon})$ the subgrid heat flux vector and σ the non-mechanical energy supply, which henceforth will be neglected. Moreover, $\bar{p}=\bar{p}(\bar{\rho},\tilde{\varepsilon})$ and $\tilde{\varepsilon}=\tilde{\varepsilon}(\bar{\rho},\tilde{T})$, where λ, $\mu=\rho\nu$ and κ denote the coefficients of viscosity and thermal conductivity, respectively. For future reference, we note that the energy equation (5_3) can be reformulated by using the thermodynamic identity $T\mathrm{d}\eta=\mathrm{d}\varepsilon+p\mathrm{d}(\rho^{-1})=\mathrm{d}h-\mathrm{d}p/\rho$, where η is the entropy and h the enthalpy, respectively, of the fluid, so that (5_3) is replaced by the equation,

$$\bar{\rho}\tilde{T}D_t(\tilde{\eta})=\bar{\rho}\tilde{T}[\partial_t(\tilde{\eta})+\mathrm{grad}\tilde{\eta}\cdot\tilde{\mathbf{u}}]=\overline{\mathbf{S}_u\cdot\mathrm{grad}\mathbf{u}}+\mathrm{div}(\bar{\mathbf{h}}-\mathbf{b}), \tag{6}$$

where $\bar{p}=\bar{p}(\bar{\rho},\tilde{\eta})$ and $D_t(\cdot)=\partial_t(\cdot)+\tilde{\mathbf{u}}\cdot\mathrm{grad}(\cdot)$ denotes the material time derivative. Similarly, for an incompressible isothermal viscous fluid with (constant) density ρ_0, the governing equations are,

$$\begin{cases} \rho_0[\mathrm{div}\bar{\mathbf{v}}]=0, \\ \rho_0[\partial_t(\bar{\mathbf{v}})+\mathrm{div}(\bar{\mathbf{v}}\otimes\bar{\mathbf{v}})]=-\mathrm{grad}\bar{\pi}+\mathrm{div}(\overline{\mathbf{S}_v}-\mathbf{B}_v)+\bar{\mathbf{f}}, \end{cases} \tag{7}$$

where ρ_0 is the constant density, $\mathbf{v}$ the (incompressible) velocity, $\mathbf{S}_v=\rho_0\nu(\mathrm{grad}\mathbf{v}+\mathrm{grad}\mathbf{v}^T)$ the viscous stress tensor, π the pressure, $\mathbf{B}_v=\rho_0(\overline{\mathbf{v}\otimes\mathbf{v}}-\bar{\mathbf{v}}\otimes\bar{\mathbf{v}})$ the subgrid stress tensor, and $\mathbf{f}$ the specific body force, which will be neglected in analogy with the compressible case. The equation-of-state for the incompressible pressure can thus be expressed as $\bar{\pi}=p(\rho_0,\bar{\eta})$, where η is the entropy of the incompressible fluid, from which we further conclude that $\bar{\pi}=\bar{\pi}(\bar{\eta})$.

Assuming that (7) can be solved for the flow of interest, given a subgrid model and appropriate initial and boundary conditions, it is natural to define the acoustic components (or fields) as the difference between the compressible and the incompressible components (or fields),

$$\rho'=\bar{\rho}-\rho_0,\ \ \mathbf{v}'=\tilde{\mathbf{u}}-\bar{\mathbf{v}},\ \ p'=\bar{p}-\bar{\pi},\ \ \eta'=\tilde{\eta}-\bar{\eta}, \tag{8}$$

where $\{\rho',\mathbf{v}',p'\}$ denotes the acoustic components of the density, velocity and pressure, respectively. When $|p'|<<\rho_0c_0^2$, we have no heating by shock waves, i.e. $\eta'=0$, and the entropy in the incompressible case equals that of the compressible case. The governing equations for $\{\rho',\mathbf{v}',p'\}$ can be obtained by combining (5), with (5_3) replaced by (6), and (7), using the definitions (8), to give the following non-linear acoustic equations,

$$\begin{cases} \partial_t(\rho')+\rho_0\mathrm{div}\mathbf{v}'+\mathrm{grad}\rho'\cdot\bar{\mathbf{v}}+\mathrm{div}(\rho'\mathbf{v}')=0, \\ \partial_t(\rho_0\mathbf{v}'+\rho'(\bar{\mathbf{v}}+\mathbf{v}'))+\rho_0\mathrm{div}(\bar{\mathbf{v}}\otimes\mathbf{v}'+\mathbf{v}'\otimes\bar{\mathbf{v}}+\mathbf{v}'\otimes\mathbf{v}')+\mathrm{div}(\rho'((\bar{\mathbf{v}}+\mathbf{v}')\otimes(\bar{\mathbf{v}}+\mathbf{v}'))) \\ \qquad =-\mathrm{grad}p'+\mathrm{div}[(\overline{\mathbf{S}_u}-\overline{\mathbf{S}_v})-(\mathbf{B}_u-\mathbf{B}_v)]. \end{cases} \tag{9}$$

The combined viscous and subgrid term, $\mathrm{div}[(\overline{\mathbf{S}_u}-\overline{\mathbf{S}_v})-(\mathbf{B}_u-\mathbf{B}_v)]$, on the right-hand-side of (9) can be reformulated by using (8_2), (7_1) and the definition $\mu=\rho_0\nu$ to give,

$$\begin{cases}\delta\overline{\mathbf{S}}=\overline{\mathbf{S}_u}-\overline{\mathbf{S}_v}=(\lambda+\frac{2}{3}\rho_0\nu)\mathrm{div}\mathbf{v}'+\rho_0\nu(\mathrm{grad}\mathbf{v}'+\mathrm{grad}\mathbf{v}'^{\mathrm{T}}),\\ \delta\mathbf{B}=\mathbf{B}_u-\mathbf{B}_v\approx\mathbf{B}_u^{\mathrm{EVM}}-\mathbf{B}_v^{\mathrm{EVM}}=-2\mu_k\tilde{\mathbf{D}}_D-(-2\rho_0\nu_k\overline{\mathbf{D}})\approx-\rho_0\nu_k(\mathrm{grad}\mathbf{v}'+\mathrm{grad}\mathbf{v}'^{\mathrm{T}}),\end{cases} \tag{10}$$

where we have assumed that the subgrid model chosen is of eddy-viscosity type (cf. 2), and that the eddy viscosities ν_k and μ_k, respectively, are related in such a way that $\mu_k=\rho_0\nu_k$. Furthermore, by introducing the linear combination $\mathbf{w}=\rho_0\mathbf{v}'+\rho'(\overline{\mathbf{v}}+\mathbf{v}')$ equation (9) simplifies to,

$$\begin{cases}\partial_t(\rho')+\mathrm{div}(\mathbf{w})=0,\\ \partial_t(\mathbf{w})+\mathrm{div}(\mathbf{w}\otimes(\overline{\mathbf{v}}+\mathbf{v}')+\rho_0\overline{\mathbf{v}}\otimes\mathbf{v}')=-\mathrm{grad}p'+\mathrm{div}[\delta\overline{\mathbf{S}}-\delta\mathbf{B}].\end{cases} \tag{11}$$

In order to be closed the equations (11) must be supplemented by a relation between p', ρ' and $\overline{\pi}$. When $\tilde{\eta}=\overline{\eta}$ and $\overline{\eta}=\overline{\eta}(\overline{\pi})$ the equation-of-state for the fluid can be expressed as $\overline{p}=\overline{p}(\rho_0+\rho',\overline{\pi})$. Equation (8a) then yields $p'=\overline{p}(\rho_0+\rho',\overline{\pi})-\overline{p}(\rho_0,\overline{\pi})$, which, by means of a Taylor series expansion, results in the expression,

$$p'=c^2\rho'+O((\rho')^2), \tag{12}$$

where $c^2=(\partial\overline{p}/\partial\overline{\rho})_{\rho'=0}=c^2(\overline{\pi})$ defines the speed of sound in the fluid in the limit of vanishing dilatation (or compression). Experimental studies, [20], give for the pressure dependence,

$$c^2=c_{atm}^2+G_0(\overline{\pi}-p_{atm})/\rho_0, \tag{13}$$

valid up to about 50 MPa, where G_0 is around 5 and c_{atm} is the speed of sound at atmospheric pressure p_{atm}. Introducing $c_0^2=c_{atm}^2-G_0p_{atm}/\rho_0$ we have $c^2=c_0^2+G_0\overline{\pi}/\rho_0$ Inserting this in (12) yields,

$$p'=(c_0^2+G_0\overline{\pi}/\rho_0)\rho'+O(\rho'). \tag{14}$$

Differentiating expression (14) yields,

$$\delta p'=(c_0^2+G_0\overline{\pi}/\rho_0)\delta\rho'+G_0(\rho'/\rho_0)\delta\overline{\pi}+O(\rho'). \tag{15}$$

By combining the time derivative of (11_1) and the divergence of (11_2), using equation (12) or rather the simplified version of (15), an inhomogeneous wave-equation for ρ' is obtained,

$$\tilde{\circ}(\rho')=\partial_t^2(\rho')-\mathrm{div}(c^2\mathrm{grad}\rho')=\mathrm{div}(\mathrm{div}\mathbf{T})+\mathrm{div}(G_0(\rho'/\rho_0)\mathrm{grad}\overline{\pi}), \tag{16}$$

where $\tilde{\circ}(\cdot)=\partial_t^2(\cdot)-\mathrm{div}(c^2\mathrm{grad}(\cdot))$ and the r.h.s. is given by a double divergence of the term,

$$\begin{aligned}\mathbf{T}&=\mathbf{w}\otimes(\overline{\mathbf{v}}+\mathbf{v}')+\rho_0\overline{\mathbf{v}}\otimes\mathbf{v}'-(\delta\overline{\mathbf{S}}-\delta\mathbf{B})\\ &=\mathbf{w}\otimes(\overline{\mathbf{v}}+\mathbf{v}')+\rho_0\overline{\mathbf{v}}\otimes\mathbf{v}'-((\lambda+\tfrac{2}{3}\rho_0\nu)\mathrm{div}\mathbf{v}'+\rho_0(\nu-\nu_k)(\mathrm{grad}\mathbf{v}'+\mathrm{grad}\mathbf{v}'^{\mathrm{T}})),\end{aligned} \tag{17}$$

and a correction term of generalized Laplace-type. Contrary to what is first believed, this term may be of considerable importance even if $\rho'/\rho_0<<1$ for the amplitude, phase shift and wave form of ρ'. In the same manner, another inhomogeneous wave-equation can be obtained for p', viz.,

$$\circ(p')=\partial_t(c^{-2}\partial_t(p'))-\mathrm{div}(\mathrm{grad}p')=\mathrm{div}(\mathrm{div}\mathbf{T})+\partial_t(c^{-2}G_0(\rho'/\rho_0)\partial_t(\overline{\pi})), \tag{18}$$

where $\circ(\cdot)=\partial_t(c^{-2}\partial_t(\cdot))-\mathrm{div}(\mathrm{grad}(\cdot))$. For our purposes it is more natural to consider p' as dependent variable and we thus use (18) in the rest of this study. When the noise emitter is a turbulent boundary layer, as will be the case for a surface ship and a submarine, the source region is of limited size, and outside of the boundary layer the right-hand-side of (18) is zero. For low turbulent Ma-numbers the turbulent fluctuations have little effect on sound propagation, so that the sound can propagate through the fluid as the medium were undisturbed. Hence,

$$\begin{cases}\circ(p')=\partial_t(c^{-2}\partial_t(p'))-\mathrm{div}(\mathrm{grad}p')=\mathrm{div}(\mathrm{div}\mathbf{T})+\partial_t(c^{-2}G_0(\rho'/\rho_0)\partial_t(\bar{\pi})), & \text{within } \mathrm{V}\ ,\\ \circ(p')=c_0^{-2}\partial_t^2(p')-\mathrm{div}(\mathrm{grad}p')=0, & \text{outside } \mathrm{V}\ ,\end{cases} \tag{19}$$

where the source volume V is implicitly defined by the r.h.s of (19_1). The physics involved in this term includes convection, subgrid turbulence and viscous stresses, all of which are important in different parts of the boundary layer. This term can be decomposed into its parts, and analyzed in order to determine which mechanism gives rise to different parts of the pressure wave. This is of interest mainly to minimize the hydrodynamic noise from a submarine, and will not be further elaborated on here. In order to solve (20) we therefore first have to compute (18), which in turn, requires the solution of (11) for the primary acoustic variables ρ' and $\mathbf{v}'$.

The full acoustic model (consisting of equations (11), (17) and (19)) is non-linear, but may be simplified by assuming Stokes relation $3\lambda+2\rho_0\nu=0$ and $\mathbf{T}$ to be linear in ρ' and $\mathbf{v}'$,

$$\begin{aligned}&\circ(p')=\partial_t(c^{-2}\partial_t(p'))-\mathrm{div}(\mathrm{grad}p')=\mathrm{div}(\mathrm{div}\mathbf{T})+\partial_t(c^{-2}G_0(\rho'/\rho_0)\partial_t(\bar{\pi})),\\ &\text{where}\quad \mathbf{T}=\rho'(\bar{\mathbf{v}}\otimes\bar{\mathbf{v}})+\rho_0[\bar{\mathbf{v}}\otimes\mathbf{v}'+\mathbf{v}'\otimes\bar{\mathbf{v}}+(\nu-\nu_k)(\mathrm{grad}\mathbf{v}'+\mathrm{grad}\mathbf{v}'^{\mathrm{T}})],\\ &\text{and}\quad \mathrm{K}=\mathrm{div}(\mathrm{div}\mathbf{T})+\partial_t(c^{-2}G_0(\rho'/\rho_0)\partial_t(\bar{\pi})),\end{aligned} \tag{20}$$

where the primary acoustic variables ρ' and $\mathbf{v}'$ satisfies the linearized equations,

$$\begin{cases}\partial_t(\rho')+\mathrm{grad}\rho'\cdot\bar{\mathbf{v}}+\rho_0\mathrm{div}\mathbf{v}'=0,\\ \partial_t(\rho'\bar{\mathbf{v}}+\rho_0\mathbf{v}')+\mathrm{div}(\rho'\bar{\mathbf{v}}\otimes\bar{\mathbf{v}}+\rho_0(\bar{\mathbf{v}}\otimes\mathbf{v}'+\mathbf{v}'\otimes\bar{\mathbf{v}}))=\\ \qquad -\mathrm{grad}[(c_0^2+G_0\bar{\pi}/\rho_0)\rho']+\mathrm{div}[(\nu-\nu_k)(\mathrm{grad}\mathbf{v}'+\mathrm{grad}\mathbf{v}'^{\mathrm{T}})].\end{cases} \tag{21}$$

The equations (21) are linear in ρ' and $\mathbf{v}'$, given the (incompressible) velocity field $\bar{\mathbf{v}}$, and are therefore easy to solve in comparison to the full non-linear NSE.

Considering far-field sound propagation in isotropic unrestricted waters, unrestricted waters, and littoral waters a very important consideration, besides the local variations in the speed of sound that are due to temperature, density and salinity, is the reflections from the sea-bed, which may be composed of layered material with different properties. In isotropic unrestricted waters the inhomogeneous wave equation (21) can be solved analytically, whereas in non-isotropic unrestricted waters and in littoral waters special techniques must be developed in order to account for the variations in c and the reflections in the sea-bed. In the simplest case of isotropic unrestricted waters Green's function of the inhomogeneous wave equation (20) satisfies,

$$(\partial_t^2-c^2\Delta)G(\mathbf{x},t;\mathbf{x}',t')=\delta(\mathbf{x}-\mathbf{x}')\delta(t-t'), \tag{22}$$

where δ is the Dirac function, $c=c_0$, and where G is found to be (e.g. Morse & Feshbach, [21]),

$$G(\mathbf{x},t;\mathbf{0},0)=(4\pi c^2)^{-1}\delta(t_r)|\mathbf{x}|^{-1}, \tag{23}$$

where t_r is the retarded time $t_r=t-|\mathbf{x}-\mathbf{x}'|/c$. For the problem at hand, i.e. equation (20), shows that the emitter(s) behave like quadrupoles, and the corresponding solution for the far field is,

$$\begin{aligned} p'(\mathbf{x},t)=p_1(\mathbf{x},t)+\tfrac{1}{4\pi}\iint_A\left(\tfrac{1}{|\mathbf{x}-\mathbf{x}'|}\tfrac{\partial}{\partial\mathbf{n}'}p'(\mathbf{x},t_r)\right)dS'- \\ -\tfrac{1}{4\pi}\iint_A\left(\tfrac{(\mathbf{x}-\mathbf{x}')\mathbf{n}'}{|\mathbf{x}-\mathbf{x}'|^2}\left(\tfrac{1}{|\mathbf{x}-\mathbf{x}'|}p'(\mathbf{x},t_r)+c^{-1}\tfrac{\partial}{\partial t}p'(\mathbf{x},t_r)\right)\right)dS', \end{aligned} \tag{24}$$

where we have introduced,

$$p_1(\mathbf{x},t)=\tfrac{1}{4\pi}\iiint_V\left(K(\mathbf{x}',t_r)/|\mathbf{x}-\mathbf{x}'|\right)dV', \tag{25}$$

and where **n** denotes the normal to hull of the body considered. In order to describe the noise emitter, we hence need the source term $K=K(\mathbf{x},t)$ and the pressure acting on the hull. Note that in the source term we adopt the retarded time t_r since otherwise we eliminate the possible interference of signals that arrive simultaneously at **x** but that were emitted from different locations **x** within the volume V. For an estimate of how the hydrodynamic noise scales with the characteristic flow parameters we assume that **T** and $\bar{\pi}$ scale with $\rho_0U_0^2$, where U_0 is the speed of the ship. The time scale will thus be proportional to δ/U_0, where δ is the boundary layer thickness, whereas the volume of integration scales with δRL, where L is the length of the ship and R is the hydraulic radius. Accordingly, the pressure scales as $p'\propto Ma^2(\rho_0U_0^2)(RL/r\delta)$.

4. Numerical Methods

LES requires high-order schemes to avoid masking the subgrid term by the leading order truncation error. In general, Δ is related to the grid, i.e. $\Delta\propto|\mathbf{d}|$, where $|\mathbf{d}|$ is the grid size, which makes the modeled subgrid stresses $O(|\mathbf{d}|^2)$ terms. In LES, spectral and high-order finite volume, element or difference methods are used for spatial discretization, whilst explicit semi-implicit or predictor-corrector methods are used for time-integration. For complex geometries the Finite Volume (FV) method is the most convenient technique. In the FV method, the domain D is partitioned into cells Ω_P so that $\cup_P(\Omega_P)=D\cup\partial D$ and $\cap_P(\Omega_P)=\varnothing$. The cell-average of f over the P^{th} cell is $f_P=\frac{1}{\delta V}\int_\Omega f dV$ so that Gauss theorem may be used to formulate the semi-discretized LES-equations. By integrating these over time, using e.g. a multi-step method, [22], the discretized LES-equations become,

$$\begin{cases} \frac{\beta_i\Delta t}{\delta V_P}\sum_f[F_f^{C,\rho}]^{n+i}=0, \\ \sum_{i=0}^{m}(\alpha_i(\bar{\mathbf{v}})_P^{n+i}+\frac{\beta_i\Delta t}{\delta V_P}\sum_f[\mathbf{F}_f^{C,v}+\mathbf{F}_f^{D,v}+\mathbf{F}_f^{B,v}]^{n+i})=-\beta_i(\mathrm{grad}\bar{p})_P^{n+i}\Delta t, \end{cases} \tag{26}$$

where m, α_i and β_i are parameters of the multi-step method, whereas,

$$F_f^{C,\rho}=(\bar{\mathbf{v}}\cdot d\mathbf{A})_f,\ \mathbf{F}_f^{C,v}=(\bar{\mathbf{v}}\cdot d\mathbf{A})_f\bar{\mathbf{v}}_f,\ \mathbf{F}_f^{D,v}=(\nu\mathrm{grad}\bar{\mathbf{v}})_f d\mathbf{A},\ \mathbf{F}_f^{B,v}=(\mathbf{B})_f d\mathbf{A}, \tag{27}$$

are the convective, viscous and subgrid fluxes. To close the FV-discretization the fluxes (at face f) need to be reconstructed from the variables at adjacent cells. This requires flux interpolation for the convective fluxes and difference approximations for the inner derivatives of the viscous and subgrid fluxes, $\mathbf{F}_f^{D,v}$ and $\mathbf{F}_f^{B,v}$, respectively. Typically, for second order accuracy,

$$\begin{cases} \mathbf{F}_f^{D,v}=\nu|d\mathbf{A}|(\bar{\mathbf{v}}_N-\bar{\mathbf{v}}_P)/|\mathbf{d}|+\frac{1}{6}\nu(\mathbf{d}\otimes\mathbf{d})\nabla^3\bar{\mathbf{v}}, \\ \mathbf{F}_f^{C,v}=F_f^{C,\rho}\bar{\mathbf{v}}_f=F_f^{C,\rho}(1\bar{\mathbf{v}}_P+(1-1)\bar{\mathbf{v}}_N-\frac{1}{8}(\mathbf{d}\otimes\mathbf{d})\nabla^2\bar{\mathbf{v}}), \end{cases} \tag{28}$$

where $\frac{1}{6}\nu(\mathbf{d}\otimes\mathbf{d})\nabla^3\bar{\mathbf{v}}$ and $-\frac{1}{8}(\mathbf{d}\otimes\mathbf{d})\nabla^2\bar{\mathbf{v}}$ represent the leading order truncation errors. The equations (28) can be decoupled by combining (28_1) and (28_2) into a Poisson equation for $\bar{p}$, which is to be solved together with (28_2). The scalar equations are usually solved sequentially with iteration over the explicit coupling terms to obtain convergence. The segregated approach yields a Courant (Co) number restriction with Co<0.5, but a value of Co≈0.2 is preferable since LES attempts to resolve the dynamics of the smallest resolvable structures with a size of O(Δ).

The acoustic equations (20) and (21) are discretized using the same methodology as for the LES-equations. More precisely, the inhomogeneous wave equation (20) becomes,

$$\begin{aligned} c^{-2}[(p')_P^{n+2}-2(p')_P^{n+1}+(p')_P^{n}]-\tfrac{\Delta t^2}{\delta V_P}\textstyle\sum_f[(\mathrm{grad}p')_f]^{n+2}=\tfrac{\Delta t^2}{\delta V_P}\textstyle\sum_f[(\mathrm{div}\mathbf{T})_f]^{n+2}+ \\ +(c^{-2}\Gamma_0(\rho'/\rho_0))[(\bar{\pi})_P^{n+2}-2(\bar{\pi})_P^{n+1}+(\bar{\pi})_P^{n}] \end{aligned} \tag{29}$$

where the inner derivatives in **T** are replaced by central difference approximations of second order accuracy, and whereas the linear equations for the acoustic variables ρ' and $\mathbf{v}'$ becomes,

$$\begin{cases} \sum_{i=0}^{m}(\alpha_i(\rho')_P^{n+i}+\frac{\beta_i\Delta t}{\delta V_P}\sum_f[\mathbf{F}_f^{C}]^{n+i})=\beta_i(\rho_0\mathrm{div}\mathbf{v}')_P^{n+i}\Delta t, \\ \sum_{i=0}^{m}(\alpha_i(\rho'\bar{\mathbf{v}}+\rho_0\bar{\mathbf{v}}')_P^{n+i}+\frac{\beta_i\Delta t}{\delta V_P}\sum_f[\mathbf{F}_f^{C,\rho'}+\mathbf{F}_f^{C,\rho_0}+\mathbf{F}_f^{D,B}]^{n+i})=-\beta_i(\mathrm{grad}((c_0^2+G_0\bar{\pi}/\rho_0)\rho'))_P^{n+i}\Delta t, \end{cases} \tag{30}$$

where $\mathbf{F}_f^{C}=(\rho'\bar{\mathbf{v}}\cdot d\mathbf{A})_f$ is the convective flux function in (21_1) and $\mathbf{F}_f^{C,\rho_0}=\rho_0((\mathbf{v}'\cdot d\mathbf{A})_f\bar{\mathbf{v}}_f+(\bar{\mathbf{v}}\cdot d\mathbf{A})_f\mathbf{v}_f')$, $\mathbf{F}_f^{C,\rho'}=(\rho'\bar{\mathbf{v}}\cdot d\mathbf{A})_f\bar{\mathbf{v}}_f$, and $\mathbf{F}_f^{D,B}=((\nu-\nu_k)(\mathrm{grad}\mathbf{v}'+\mathrm{grad}\mathbf{v}'^{T}))_f d\mathbf{A}$ are the convective and viscous fluxes in the linear equations (21_2). The scalar equations are solved sequentially with iteration over the explicit coupling terms to obtain convergence, with a time-step limitation of Co<0.2.

5. The Flow Around an Inclined Prolate Spheroid

A complex flow of great interest to the aeronautical and marine communities is the flow past a 6:1 prolate spheroid at incidence. This type of flow has been studied both experimentally, [23-25], and numerically, [26-27], for various angles of attack and body-length Re-numbers. From the experimental studies it is well-known that at low angles of attack ($\alpha<20°$) the flow separates on the afterbody whereas at high angles of attack ($\alpha\geq20°$) the flow separates on the leeward side proximate to the nose region. In the present investigation, extending the work of Hedin et al, [28], we focus on $\alpha=20°$ and a body-length Re-number of $4.2\cdot10^6$. The computational domain consist of a rectilinear model of the wind-tunnel, with the same hydraulic radius as the tunnel used in the experiments, in which the prolate spheroid is mounted. The grid consists of two blocks: an inner O-type grid that wraps around the spheroid and an outer O-type grid that fills the region between the inner grid and the wind-tunnel walls. Figure 1 shows a perspective view of the computational domain together with representative grid surfaces. The grid is concentrated around the prolate spheroid, in order to capture as much as possible of the boundary layer, having a wall-normal-distance of $y^+\approx90$, where $y^+=u_\tau y/\nu$, in which $u_\tau=\tau_w^{1/2}$ is the friction velocity, τ_w the wall-shear-stress, and y the distance to the wall. Two grids have been constructed, with the coarse grid including some 500,000 cells and the fine grid some 1,000,000 cells. In the present study, we only aim at demonstrating the computational method for flow induced noise, and we therefore only use results from the coarse grid. At the inlet, $\bar{\mathbf{v}}=\mathbf{v}_\infty$ and $\partial\bar{p}/\partial\mathbf{n}=\mathbf{0}$, where **n** is the outward unit normal, at the outlet, $\partial(\bar{\mathbf{v}}\cdot\mathbf{n})/\partial\mathbf{n}=\mathbf{0}$ and $\bar{p}=p_\infty$, and at the windtunnel walls slip conditions are used and at the hull no-slip conditions are used. The LES calculations are initiated with quiescent conditions and the unsteady flow

evolved by itself. Different subgrid turbulence models, including different versions of SMG and OEEVM are being evaluated and other models, besides the most common LES subgrid models will be evaluated on this case due to its complexity, and in particular its demands on accurate handling of grid and flow anisotropies, which has proven very complicated, cf. [4].

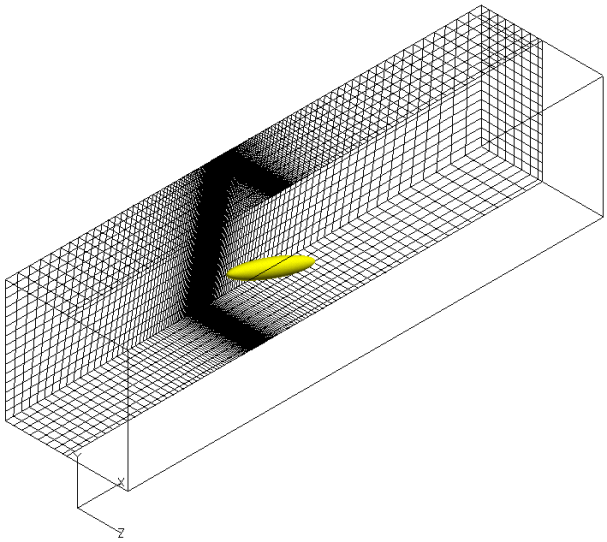

Figure 1. Perspective view of the computational domain and the grid system used. Note the refinement of the mesh towards the hull of the prolate shperoid.

5.1. Global Flow Features

Figure 2 presents perspective views of the flow at $\alpha=20°$ in terms of instantaneous (a) and time-averaged (b) streamtubes released at arbitrary locations just above the hull. The streamtubes are obtained from the resolved velocity field by integrating the equation $d\bar{\mathbf{v}}(\mathbf{x},s,t)/ds=\dot{\bar{\mathbf{v}}}(\mathbf{x},s,t)$, where s is the arc-length coordinate and where the dot denotes the material time-derivative. The integration is carried out using a fourth-order accurate Runge-Kutta method. The streamribbons clearly show the complexity of flow and the difference between the mean flow and the instantaneous flow. On the windward side, an attached three-dimensional boundary layer is formed, which detaches from the hull on the leeward side as a result of the circumferential adverse pressure gradient and roll-up into a counter-rotating pair of longitudinal vortices on the back of the body. Below these primary vortices a pair of counter-rotating secondary vortices can also be observed. By comparing figure 2a and 2b the variations in the flow, as well as the dynamics of the separation line, can be found. On average, fluid from the windward side is convected across the ellipsoid, engulfed into the primary vortices, and finally ejected into the near-wake. The primary vortices are symmetric with respect to the body in the mean, and appear fairly stationary for different angles of attack. Transition occurs naturally at $x_1/L\approx0.15\pm0.02$ on the forebody, depending on the subgrid model. In the experiments the flow was tripped at $x_1/L\approx0.20$, using a tripp wire, forcing the transition to occur at this location. It is likely that the difference in transition affects the distance between the primary vortices and the hull at all downstream locations. Since transtion occurs too early in the computations, the predicted primary vortices should be expected to be located further from the hull than what is found in the experiments. In turn, this would also alter the pressure distribution on the hull itself. The qualitative agreement between the predicted and measured flow is however satisfactory taking into account the complexity of the flow, the differences due to fixed and natural transition, and the simple subgrid models used. In particular, trends related to incidence effects, [28], i.e. the roll-up of fluid and subsequent formation of the vortices, and the associated flow features are well captured.

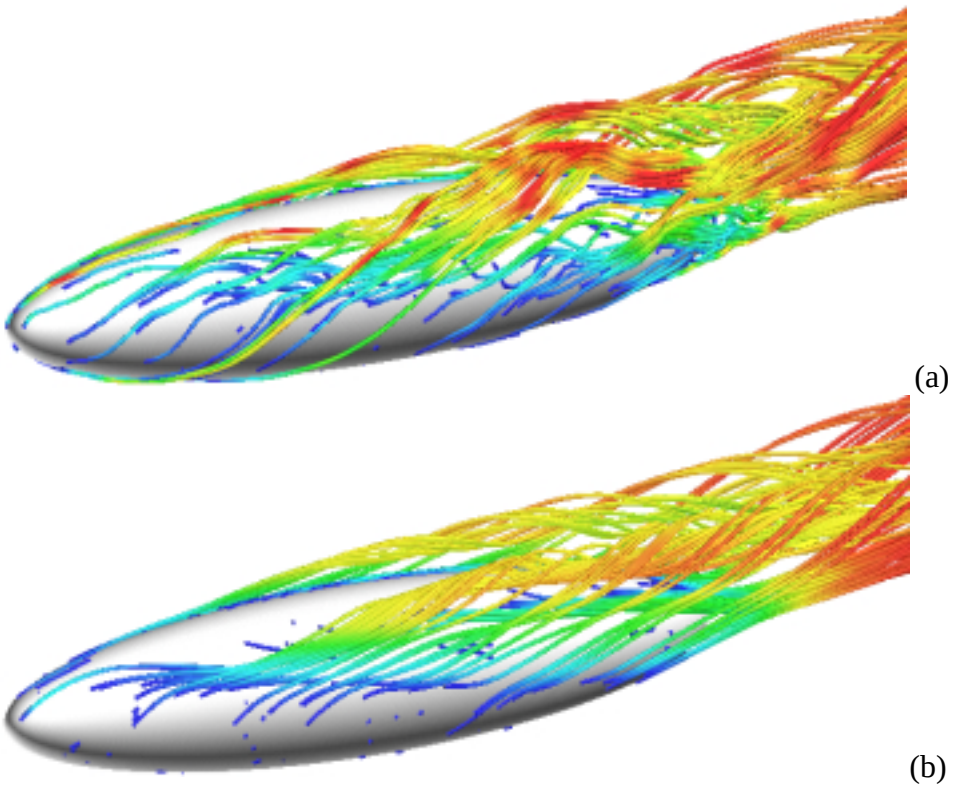

Figure 2. Instantaneous (a) and time-averaged (b) perspective views of the flow around the prolate spheroid in terms of streamtubes released at a small distance (y^+=O(25)) above the hull. The streamtubes are colored by the instantaneous and time-averaged streamwise velocities, respectively.

Figure 3 shows secondary streamlines superimposed on contours of the time-averaged velocity magnitude $|\mathbf{v}|$ and contour lines of the resolvable turbulent kinetic energy $k=\frac{1}{2}(\langle\mathbf{v}^2\rangle-\langle\mathbf{v}\rangle^2)$ at (a) x/L=0.600 and (b) x/L=0.772, respectively. Here, x is the major axial distance from the nose and L the total length of the ellipsoid. The highest fluid velocity is found to be on the side of the ellipsoid ($\varphi\approx90°$), where the flow has accelerated around the model, and underneath the primary vortex. The lowest velocities are found just downstream of the separation lines. Moreover, a trough of low-velocity fluid can be observed between the two separation lines corresponding to regions with large values of v_{rms} and low values of p_{rms}. The explanation for this trough of low-velocity downstream of the separation lines is that the primary vortices sweep up the low momentum fluid in the vicinity of the wall and that this fluid then accumulates between the primary vortex itself and the separation line. Some of the low-velocity fluid gets pulled out of the region near the wall and into the vortex itself. This can be observed in figure 3b where a finger of low-velocity fluid stretches from the wall out towards the core of the vortex. The contours of k indicate that the lifting of the secondary streamlines at separation is accompanied by the lifting of a sheet of turbulent fluid. This sheet appears to be drawn by the primary vortex from the boundary layer into the vortex core. The regions of maximum k correspond to regions of low momentum fluid (i.e. low velocity magnitude, $|\mathbf{v}|$) that also is associated with the downstream corner of the primary vortex.

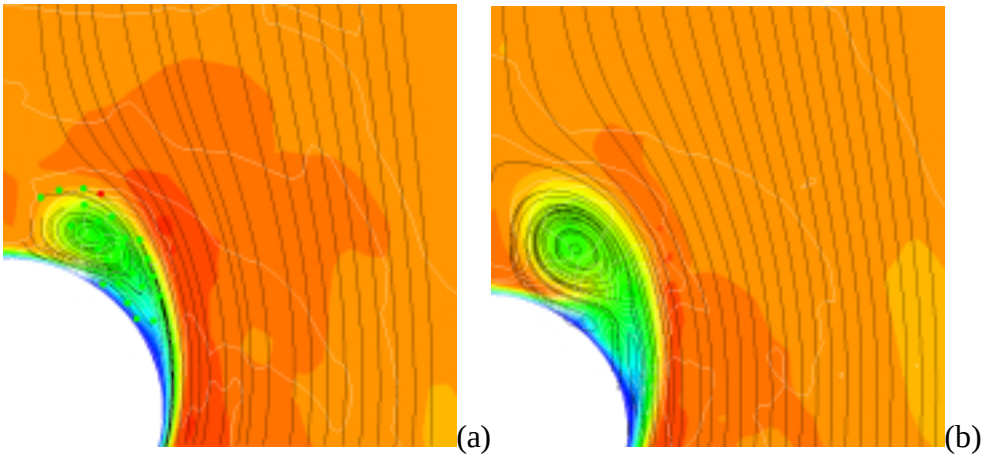

Figure 3. Secondary streamlines (black) superimposed on contours of the time-averaged velocity magnitude $|\bar{\mathbf{v}}|$ and contour lines (white) of the resolvable turbulent kinetic energy $k=\frac{1}{2}(\langle \mathbf{v}^2 \rangle - \langle \mathbf{v} \rangle^2)$ at (a) x/L=0.600 and (b) x/L=0.772, respectively.

5.2. Comparison with Experimental Data

Figure 4 presents the measured and predicted secondary velocity field at x/L=0.600 and x/L=0.772 from LES using SMG and OEEVM. We first notice that the difference between the subgrid models is virtually insignificant, and we therefore focus our comparision with the experimental data on the OEEVM model. At x/L=0.600 the predicted primary vortex is considerably stronger than in the experiments. The reason for this is believed to be the early transition, but an additional reason may be that the eddy-viscosity subgrid models overpredicts the viscosity in the first cell, and therefore also the thickness of the boundary layer. At x/L=0.772 the primary vortex is located at 3.6 cm above the hull surface at φ=155°, which is to be compared with the experimental values of 3.1 cm above the hull surface at φ=155°, which corroborates the previous conclusions. In addition, the secondary vortex is located at φ=140° in both the simulations and the experiments. The associated separation lines are at φ=118° and φ=142°, respectively, which is in good agreement with the experimental values of φ=112° and φ=135°, respectively. By comparing measured and predicted pressure coefficients C_p at x/L=0.600 and x/L=0.772 it appears that the primary vortex is located too far from the hull, giving further evidence to the previous results. On the windward side the subgrid model has little or no influence on the results, whilst on the leeward side some differences can be observed between LES using different subgrid models and the measurements.

It is very hard to accurately represent the forced transition of the experiments in the computational model without resolving all details, including the tripp-wire itself. The experimentalists claim that the influence of tripping the flow at x/L=0.20 is marginal to that of a natural transition, and based on that we should seek improved subgrid models. The subgrid model must take into account the near wall effects – the best way to accomplish this appears to be by using a subgrid model that can automatically adjust the model coefficients to the local flow. A pragmatic approach would be to use van-Dreist damping functions, but this approach fails to produce the correct scaling of τ_w, and is not general enough considering the wide ranges of applicability we face. A more elaborate and general approach is to use a differential subgrid stress model, which is a more general model, capable of handling simultaneous grid and flow anisotropies. A third possibility is to alter the definition of the filter width Δ in LES to better represent the situation with strong anisotropy both in the grid (with pancake-type cells close to the hull and cube-type cells in the freestream flow). This is

however beyond the scope of the current study, but should be mentioned for completeness. At present these improvements, along with others, are being tested.

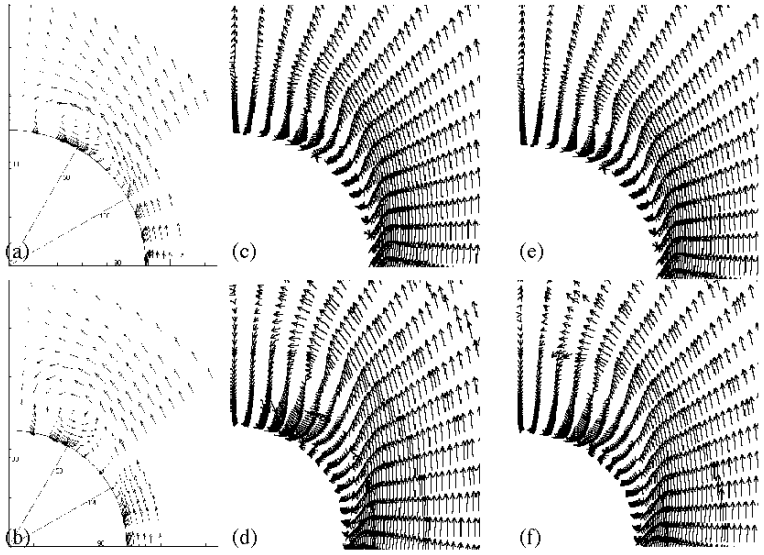

Figure 4. Comparison of measured (a, b) and predicted secondary velocity vectors at x/L=0.600 (a, c and e) and x/L=0.772 (b, d and f) for LES using SMG (c and d) and OEEVM (e and f).

5.3. Implications on Flow Induced Noise

Based on the previously discussed LES results we now aim at analyzing these databases in order to investigate the turbulent wall-pressure fluctuations, known to be an essential source for flow induced noise, and sound generation by means of the derived model (20)-(21). Again, we emphasise that this is mearly a demonstration of the model developed and not an attempt to validate its quantitative or qualitative features, for which specific experiments are required. Such a detailed validation study will, however, be performed in the near future.

Figure 5 shows the instantaneous incompressible pressure distribution (a), the time-averaged pressure distribution (b), the pressure fluctuations (c), and the rms-pressure fluctuations (d) on the hull of the prolate spheroid at an arbitrary instant in time, some time after the first order statistical moments have converged. The peak pressure is found on the windward side of the nose, wheras the minimum pressure occurs on the sides of the prolate spheroid, towards the nose region. This low pressure region coinsides well with the region of transition, which is further supported by the conjecture of Casarella, [29], suggesting that transition occurs at the point of minimum pressure for high Re-number flows. The complexity of the flow becomes apparent by comparing figures 5a and 5b, or by examining the instantaneous pressure fluctuations in 5c and the rms-pressure fluctuations in 5d. The instantaneous incompressible pressure fluctuations show patches of alternating positive and negative values, suggesting high spatio-temporal intermittency. The negative values are most frequently observed either on the windward side of the nose region or on the shoulders of the prolate spheroid, towards the downstream end of the hull. The rms-pressure fluctuations show very high values on the windward side of the nose region, and large coherent patches of low values across the rear parts of the shoulders of the prolate spheroid. Additional patches of high rms-pressure fluctuations can be observed on the back of the prolate spheroid, forming a symmetric pattern localized just below the cores of the primary vortices. Furthermore, based on the pressure distribution we get further evidence for a too early separation in the LES. This may be caused by

the subgrid turbulence model, or by the fact the the LES does not take into account that in the experiments the flow was tripped by a tripp-wire at x/L=0.20.

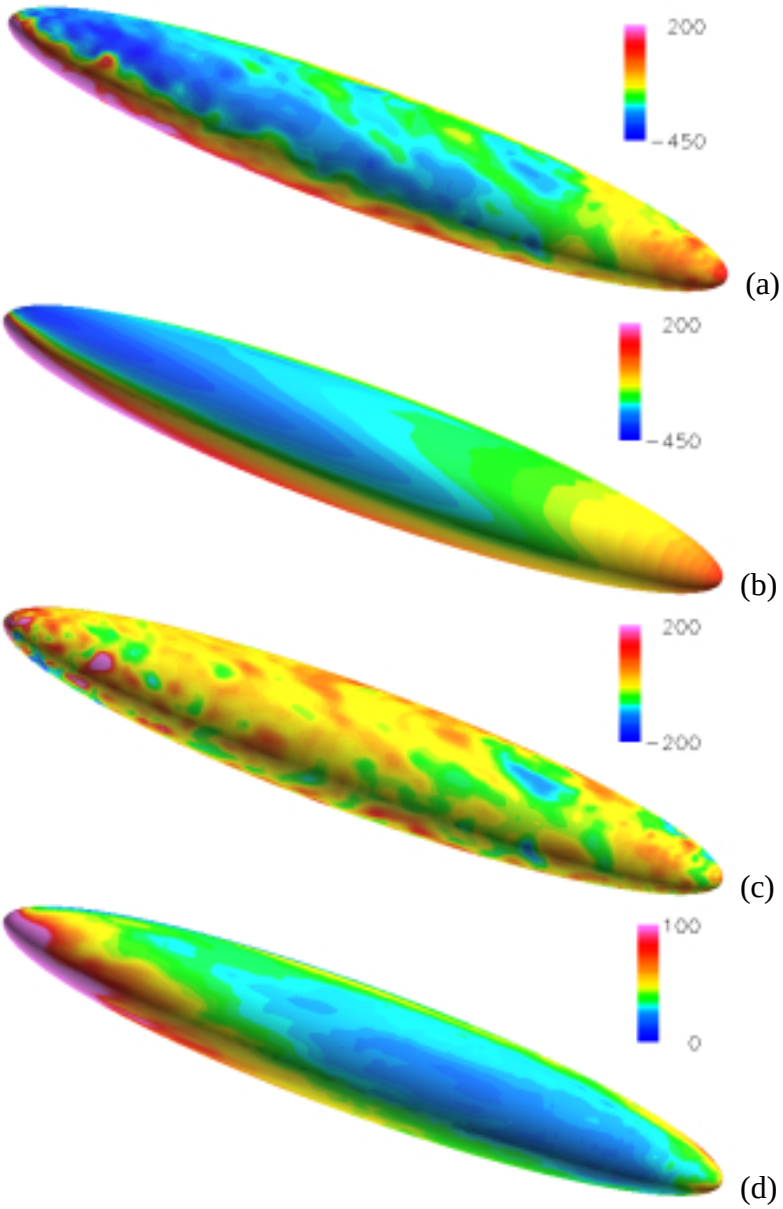

Figure 5. Characterization of the pressure distribution on the hull of the prolate spheroid: (a) instantaneous pressure, (b) time-averaged pressure, (c) pressure fluctuations and (d) rms-pressure fluctuations.

Figure 6 shows the instantaneous distribution of $K=\mathrm{div}(\mathrm{div}\mathbf{T})+\partial_t(c^{-2}G_0(\rho'/\rho_0)\partial_t(\bar{\pi}))$ on the hull of the prolate spheroid. Here, $\mathbf{T}=\rho'(\bar{\mathbf{v}}\otimes\bar{\mathbf{v}})+\rho_0[\bar{\mathbf{v}}\otimes\mathbf{v}'+\mathbf{v}'\otimes\bar{\mathbf{v}}+(\nu-\nu_k)(\mathrm{grad}\mathbf{v}'+\mathrm{grad}\mathbf{v}'^{\mathrm{T}})]$ in which ρ' and $\mathbf{v}'$ have been obtained by solving equation (21). Alternating patches of high and low values of K are observed in the nose region but also at the stern. Along the main part of the hull the peak values occur less frequently, and are often separated by coherent patches of low K-values. By inspecting either iso-surfaces of K or contour lines of K on selected planes we find that outside of the boundary layer K is virtually zero everywhere. This indicates that it is only within the turbulent boundary layer that noise is produced in terms of the source term K in the wave-equation (20). The wall-pressure fluctuations (figure 5c) show some topological similarities with K, but the correlation coefficient $r_{K,\bar{p}-\langle\bar{p}\rangle}=\mathrm{cov}[K,\bar{p}-\langle\bar{p}\rangle]/\sqrt{\mathrm{var}[K]\cdot\mathrm{var}[\bar{p}-\langle\bar{p}\rangle]}$ is less than 0.6. However, the regions of peak |K| coincides well with regions of high pressure upstream of separation (ie. in the nose re-

gion) and after complete separation (i.e. in the stern). As indicated in equations (24) and (25) both K and the pressure fluctuations on the hull itself contribute to the sound pressure levels at arbitrary location outside of the bounadry layer, which becomes similar to the the source volume V which was introduced in equation (19). An interesting observation is that the primary vortices on the back of the prolate spheroid does not give any visible imprint in K. This was also the case for the pressure fluctuations (figure 5c), but the average location of these vortices could easily be observed in the rms-pressure fluctuations (figure 5d). To this end it would be valuable also to examine the statistics of K, which however is beyond the scope of this report.

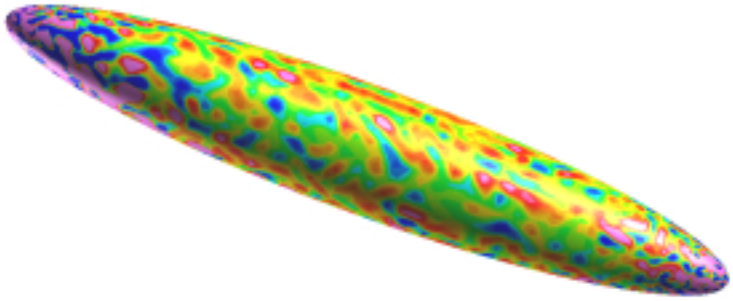

Figure 6. Instantaneous distribution of the source term $K=\mathrm{div}(\mathrm{div}\mathbf{T})+\partial_t(c^{-2}G_0(\rho'/\rho_0)\partial_t(\overline{\pi}))$ on the hull of the prolate spheroid. Dark blue corresponds to large negative values of K whereas pink corresponds to high positive values of K.

In figure 7 we present typical time-series of the incompressible pressure $\overline{\pi}$ from points within the boundary layer of the prolate spheroid and the corresponding energy spectra together with the characteristic $f^{-5/3}$ curve, significant of the inertial subrange part of the energy spectrum. The four points are all located within the boundary layer but at different positions and at different distances from the hull. We present a time sequence of 0.08s capable of resolving all frequences of interest. Figure 7a supports the previous observations (e.g. the streamline patterns in figure 2) that the flow field is dominated by large scale coherent structures and their intrinsic dynamics. However, within the boundary layer the flow alters and boundary layer turbulence is observed. The energy spectra shows a clear $f^{-5/3}$ region, indicating that the cut-off wave-number is well within the inertial subrange, suggesting that the LES computations are sufficiently well resolved, at least outside of the boundary layer. The energy spectra also show a region with a much steeper decay-rate, approximately f^{-4}. This corresponds to the modified viscous part of the spectra. Towards the high

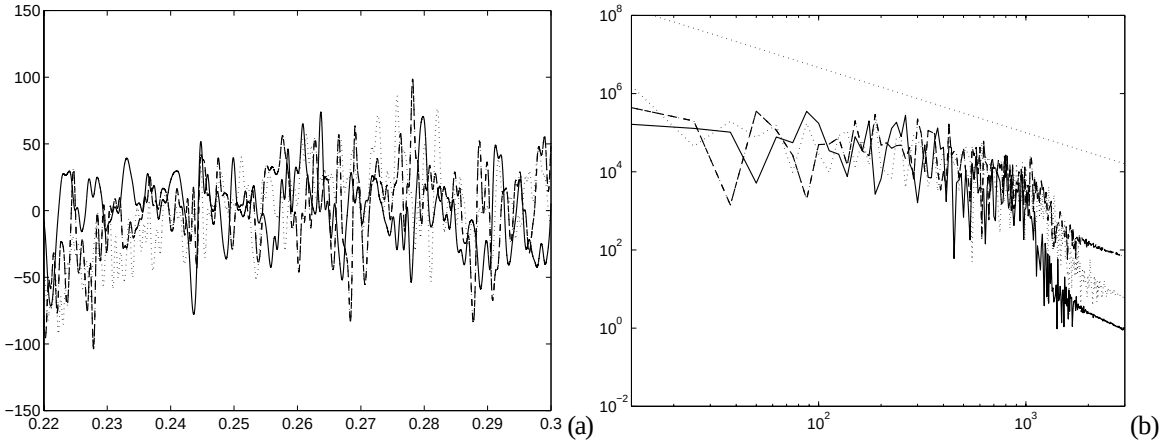

Figure 7. Time series (a) and energy spectra (b) of the incompressible pressure at four different locations within the hull boundary layer of the prolate spheroid.

wave-numbers in this area the subgrid model is active and drains kinetic energy from the system. Since most conventional subgrid models are not adapted to viscous region, this drainage is too intense, causing too much damping and a too thick boundary layer. The remedy is to use a model which can recognize the viscous subrange, see Fureby [4] for additional details.

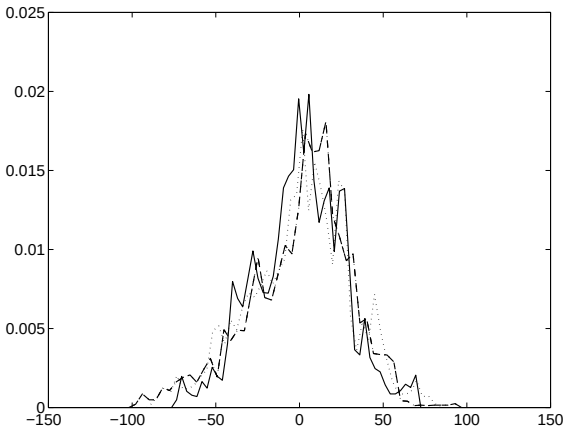

Figure 8. Probability density functions $\wp$ of the incompressible pressure at four different locations within the hull boundary layer of the prolate spheroid.

Figure 8 shows the corresponding Probability Density Functions (PDF) of $\bar{\pi}$. The probability density $\wp$ is conventionally defined according to $\frac{1}{p_0}\int\wp d\bar{\pi}=1$, and is constructed from the pressure histories sampled during the time sequence shown in figure 7. The PDFs are all quite similar, and have a typical Gaussian shape, with a variance of about 100 m^2/s^2. The corresponding variance in the velocity field is obtained from the resolvable turbulent kinetic energy k (not shown), and is approximately 7 m/s. From this value the turbulent intensity can be estimated to be about 15%. The Gaussian-shaped PDFs of the incompressible pressure (figure 8) suggests that the wall-pressure fluctuations are predominantly random, and are fairly typical of a fully developed turbulent boundary layer. In addition, the PDFs of the wall-normal velocity components (not shown) correlate well with the incompressible pressure fluctuations (figure 8), whereas the other velocity components show virtually no correlation with the incompressible pressure fluctuations.

6. Concluding Remarks

The present study is a contribution towards a better understanding of the fundamental physics on hydrodynamic noise produced by the turbulent flow around a rigid hull. Because of the prohibitive cost of direct calculation using the compressible Navier Stokes equations and the conflicting requirement for the acoustic calculation of both the viscous flow and the acoustic field, it is appropriate to perform a two-step calculation, where the incompressible flow field is calculated separately from the acoustic field. Such a two-step approach is particularly attractive for nearly incompressible flow, which is the case with ship speed less than 50 knots, since a fully compressible simulation of a virtually incompressible flow is both too expensive (since the acoustic time scale need to be properly resolved) and unnecessarily complicated. The approach taken here is that the incompressible flow field is evaluated using Large Eddy Simulation(LES). In the second step, equations for the acoustic variables are solved and the source terms for the wave equation for the acoustic pressure field are obtained. We have applied this calculation procedure to the flow around a prolate

spheroid in order to demonstrate the method. Qualitative and quantitative comparisons with experimental data concerning the hydrodynamic nose is planned for a future study.

Acknowledgements

The authors whishes to thank P.-O. Hedin at Kockums AB for performing the calculations of the prolate shperoid at an incidence used in the present study.

References

[1] Blake W.K.; 1986, “Mechanics of Flow-Induced Sound and Vibration”, Vol. I and II, Academic Press Inc.
[2] Breuer M.; 1988, "Large Eddy Simulation of the Subcritical Flow Past a Circular Cylinder: Numerical and Modeling Aspects", Int. J. Numer. Meth. Fluids, **28**, p 1281.
[3] Lillberg E. & Fureby C.; 2000, "Large Eddy Simulation of Supersonic Cavity Flow", AIAA paper 00-2411.
[4] Fureby C.; 2001, "Towards Large Eddy Simulation of Complex Flows, In Direct and Large Eddy Simulation IV, Eds. Friedrich R. & Rodi W., Kluwer, The Netherlands.
[5] Tam C.K.W.; 1998, “LES for Aeroacoustics”, AIAA Paper 98-2805.
[6] Mankbadi R.R., Hayder M.E. & Povinelli A.; 1994, “Structure of Supersonic Jet Flow and its Radiated Sound”, AIAA.J. **32**, p 523.
[7] Corcos G.M.; 1961, “The structure of Turbulent Pressure Field in Turbulent Boundary Layer Flows”, J. Fluid Mech., **18**, p 353.
[8] Viswanathan K. & Sankar L.N.; 1995, “Toward the Direct Calculation of Noise: Fluid/Acoustic Coupled Simulation”, AIAA.J., **33**, p 2271.
[9] Hardin J.C. & Pope D.S.; 1994, “An Acoustic/Viscous Splitting Technique for Computational Aeroacoustics”, Theor. Comp. Fluid Dyn., **6**, p 323.
[10] Grinstein F.F. & DeVore; 1999, “Entrainment and Thrust Vector Control with Countercurrent Rectangular Jets”, AIAA Paper 99-0165.
[11] Manning T.A., Lele S.K.; 1998, “Numerical Simulation of Shock-Vortex Interactions in Supersonic Jet Screech”, AIAA Ppaper 98-0282.
[12] Lions P.L.; 1996, "Mathematical Topics in Fluid Mechanics", Oxford Science Publications, Oxford.
[13] Launder B.E. & Spalding D.B., 1972, "Mathematical Models of Turbulence", Academic Press, London.
[14] Ghosal S. & Moin P.; 1995, "The Basic Equations for the Large Eddy Simulation of Turbulent Flows in Complex Geometry", J. Comp. Phys., **118**, p 24.
[15] Fureby C. & Tabor G.; 1997, "Mathematical and Physical Constraints on Large Eddy Simulations", J. Theoretical Fluid Dyn., **9**, p 85.
[16] Sagaut, P.; 2001, "Large Eddy Simulation for Incompressible Flows", Springer Verlag, Heidelberg.
[17] Smagorinsky J.S.; 1963, "General Circulation Experiments with Primitive Equations", Mon. Weather Rev., **91**, p 99.
[18] Schumann U.; 1975, "Subgrid Scale Model for Finite Difference Simulation of Turbulent Flows in Plane Channels and Annuli", J. Comp. Phys., **18**, p 376.
[19] Menon S. & Kim W.-W.; 1996, "High Reynolds Number Flow Simulations Using the Localised Dynamic Sub Grid Scale Model", AIAA Paper No. 96-0425.
[20] Wilson W.D.; 1960, “Equation for the Speed of Sound in Water”, J. of Acoustical Soc. of America, **32**, p 641 and 1357.
[21] Morse P.M. & Feshbach H.; 1953, “Methods of Theoretical Physics”, McGraw-Hill, New York.
[22] LeVeque R.J.;1992, "Numerical Methods for Conservation Laws", Birkhüser Verlag, Berlin.
[23] Volmers H., Kreplin H.P. Meier H.U. & Kühn A.; 1985, "Measured Mean Velocity Field Around a 1:6 Prolate Spheroid at Various Cross Sections", DFVLR IB 221-85/A 08, Göttingen, Germany.
[24] Chesnakas C.J. & Simpson R.L.; 1996, "Measurements of Turbulence Structure in the Vicinity of a 3D Separation", J. Fluids Eng., **118**, p 268.
[25] Goody M., Simpson R.L. & Engel M.; 1998, "Mean Velocity and Pressure and Velocity Spectral Measurements within a Separated Flow Around a Prolate Spheroid at Incidence", AIAA Paper 98-0630.
[26] Rosenfeld M., Wolfshtein M. & Israeli M.; 1992, "A Numerical Study of the Laminar Incompressible Flow over a 6:1 Prolate Spheroid at 10(Incidence", Int. J. Num. Meth. in Fluids, **15**, p 147.
[27] Tsai C.-Y. & Whitney A.K.; 1999, "Numerical Study of Three-Dimensional Flow Separation from a &:1 Ellipsoid", AIAA 99-0172.

[28] Hedin P.-O., Alin N., Berglund M. & Fureby C.; 2001, "Large Eddy Simulation of the Flow Around an Inclined Prolate Spheroid", AIAA Paper 01-1035.
[29] Casarella M.J., Shen J.T.C. & Bowers B.E.; 1977, “On the Evaluation of Axisymmetric Firebody Shapes for Delaying Laminar-Turbulent Transition – Part I. Background and Analysis of the Problem”, David Taylor Naval Ship R & D Center, Rep. No. 77-0074, Washington DC.